

Article

State of Health Estimation for Lithium-Ion Battery Using Partial Incremental Capacity Curve and Transfer Learning

Sheng Huang ¹, Xuemei Wang ^{1,*}, Longyun Kang ^{1,2,*}, Di Xie ^{1,3} and Xi Zhang ¹¹ School of Electric Power, South China University of Technology, Guangzhou 510641, China; 202221015266@mail.scut.edu.cn (S.H.); xiedi0813@aliyun.com (D.X.); 202221015287@mail.scut.edu.cn (X.Z.)² College of New Energy, Longdong University, Qingyang 745000, China³ Guangdong Hynn Technology Co., Ltd., Dongguan 518109, China

* Correspondence: epxmwang@scut.edu.cn (X.W.); ykang@scut.edu.cn (L.K.)

Abstract: Lithium-ion battery state of health (SOH) estimation is critical in battery management systems (BMS), with data-driven methods proving effective in this domain. However, accurately estimating SOH for lithium-ion batteries remains challenging due to the complexities of battery cycling conditions and the constraints of limited data. This paper proposes an estimation approach leveraging partial incremental capacity curves and transfer learning to tackle these challenges. First, only partial voltage segments are utilized for incremental capacity analysis, which are then fed into a stacked bidirectional gated recursive unit (SBiGRU) network, and finally, transfer learning is utilized to address issues related to limited data availability and differing data distributions. The method is further enhanced through hyperparameter optimization to refine estimation accuracy. The proposed method is validated in two publicly available datasets. For the base model, the root mean square error is 0.0033. With the transfer learning method, which utilized only 1.6% of the target domain data, the root mean square error is 0.0039. Experimental results demonstrate that the proposed method can accurately estimate SOH and works well in training and testing over different voltage ranges. The results underscore the potential of the proposed SOH estimation method for lithium-ion batteries.



Citation: Huang, S.; Wang, X.; Kang, L.; Xie, D.; Zhang, X. State of Health Estimation for Lithium-Ion Battery Using Partial Incremental Capacity Curve and Transfer Learning. *Batteries* **2024**, *10*, 324. <https://doi.org/10.3390/batteries10090324>

Academic Editor: Federico Baronti

Received: 3 August 2024

Revised: 3 September 2024

Accepted: 10 September 2024

Published: 13 September 2024



Copyright: © 2024 by the authors. Licensee MDPI, Basel, Switzerland. This article is an open access article distributed under the terms and conditions of the Creative Commons Attribution (CC BY) license (<https://creativecommons.org/licenses/by/4.0/>).

1. Introduction

Lithium-ion batteries have found extensive applications in electric vehicles and renewable energy storage systems [1,2] owing to their high energy density, prolonged cycle life, minimal self-discharge, and cost-effectiveness. However, lithium-ion batteries are constantly charged and discharged during use, resulting in the inevitable aging phenomenon of lithium-ion batteries [3], which is manifested by the decrease in capacity and the increase in internal resistance. Monitoring the state of health (SOH) of lithium-ion batteries is crucial for ensuring their stability and safety. SOH is defined as the ratio of the current maximum discharge capacity to the initial capacity [4,5] and serves as a widely adopted metric to assess battery performance.

Due to the nonlinear, time-varying nature and complex dynamics of lithium-ion batteries, the SOH cannot be obtained directly from observational measurements. Current SOH estimation methods are typically categorized into model-based and data-driven approaches. Model-based methods involve constructing accurate equivalent battery models to simulate battery behavior, such as equivalent circuit models [6], electrochemical models [7], and empirical degradation models [8]. These established models are usually combined with filter techniques [9,10] to achieve precise SOH estimation. However, model-based approaches necessitate specialized knowledge, rely heavily on accurate parameterization for model predictions, and are typically applicable only to specific types of lithium-ion batteries, limiting their generalizability across battery types.

Unlike model-based approaches, data-driven approaches can accurately estimate the SOH of lithium-ion batteries from historical data alone, without having to master the complex electrochemical mechanisms inside lithium-ion batteries. The data-driven approach establishes the mapping of HI to SOH through an algorithm, the accuracy of which is largely dependent on the quality of the selected health indicator (HI) and the learning ability of the training algorithm. The prominent data-driven techniques encompass support vector machines [11,12], Gaussian process regression [13–15], and neural network algorithms [16–24]. Literature [11] developed an SVM model with radial basis functions as kernel functions to estimate the SOH. Gaussian process (GP) regression was proposed in the literature [13] for SOH estimation, highlighting GP's advantages over other prediction methods. For the neural network methods, Lin et al. [23] proposed a method to estimate SOH based on the BP neural network. Recurrent neural network (RNN) excels at processing time series data. And as a variant of RNN, LSTM solves the problem of gradient vanishing and gradient explosion. Literature [21] proposed an LSTM-based SOH estimation method. Literature [18] utilized convolutional neural networks (CNN), which are good at adaptively extracting important features, to build a SOH estimation model. Literature [19] combined the advantages of CNN and GRU to estimate SOH. Literature [24] proposed a graph convolutional network (GCN)-based approach to estimate SOH. In addition to these, neural network algorithms such as transformer [20], deep belief network (DBN) [17], etc. are also used in SOH estimation.

With a powerful nonlinear modeling model, extracting the appropriate HI is the key to accurately estimating SOH. Among these, the more stable charging process of lithium-ion batteries is considered a significant source of HIs, as opposed to the erratic discharging behavior influenced by driving patterns and road conditions. Xiong et al. [25] identified the charging capacity within a specific voltage interval during constant-current charging as the HI. Literature [26] proposed to use the maximum radius of curvature of the current in the constant voltage stage as the HI. Literature [27] proposed the amount of isochronous voltage change during constant current charging and the amount of isochronous current change during constant voltage charging as the HI. Zhu et al. [28] extracted the relaxation voltage from post-charge data and used its variance, maximum, skewness, among other metrics, as HIs. Shen et al. [18] utilized the discrete values of voltage, current, and capacity during the charging cycle as HI.

In recent years, several studies and literature have identified incremental capacity analysis (ICA) as a highly effective method for estimating SOH. Especially in the plateau region of charging and discharging, the IC curves provide a high resolution. And it can be used to analyze the information of the battery operation process from the peak value, peak position, envelope area, and location of the curve [29–32]. Li et al. [33] used incremental capacity curves to extract features and find the best estimated HI through grey relational analysis. Literature [34] estimated the SOH of lithium-ion batteries based on the incremental capacity curve and the GPR. These feature extraction methods often rely on the complete charging process. However, in practical scenarios, due to the presence of numerous stochastic charging and discharging behaviors, the initial state of charge (SOC) is always arbitrary when the vehicle is charging. Consequently, obtaining comprehensive data on full charging and discharging cycles is challenging. Some researchers have used only partial IC curves and input them directly into the algorithmic model. Literature [23,35] used GPR and BP neural networks, respectively, to input partial incremental capacity curves directly to estimate SOH. Literature [36] and literature [37] input partial incremental capacity curves into LSTM and CNN, respectively, and explored the effect of the length and location of partial incremental capacity curves on SOH estimation. These studies preliminarily verified the feasibility of estimating SOH using partial incremental capacity curves.

However, current SOH estimation based on such data-driven approaches still faces critical challenges: the first is that the model accuracy heavily relies on a specific and large amount of charging and discharging data; the initial SOC during vehicle charging is arbitrary, leading to inconsistencies between collected and trained partial segment data. For

example, if the voltage range of the training data is in the range from 3.6 V to 3.8 V while the collected data is in the range from 3.8 V to 4.0 V, this inconsistency can significantly impact the accuracy of SOH estimation. This issue is further exacerbated by constraints stemming from data limitations. The second is that models often lack generalizability. There are often significant domain differences between training and test data, such as variations in battery types, charging and discharging rates, and ambient temperatures. This disparity makes it difficult to ensure the accuracy of model predictions across domains. Regrettably, these issues commonly coexist in practical applications. Addressing these challenges—specifically, leveraging limited partial data and enhancing generalizability in SOH estimation for lithium-ion batteries—is the primary emphasis of this paper.

To address these issues, this paper adopts a transfer learning approach to solve the domain difference problem between test data and training data to realize cross-domain distribution SOH estimation with only a limited portion of charging data. The main contributions are as follows:

(1) A method is proposed for estimating the SOH of lithium-ion batteries using partial incremental capacity (IC) curves. The study investigates the effectiveness of deriving input features from various voltage segments. This approach circumvents the necessity to analyze specific features of the IC curve and diminishes the requirement for voltage and current measurements to encompass a particular SOC range.

(2) With a transfer learning approach, it is possible to estimate the SOH across diverse battery types and different voltage segments under varying conditions, using only a small subset of the segmented data.

(3) Bayesian optimization is employed to determine the number of layers to be frozen for transfer learning while optimizing the other hyperparameters of the model in order to improve model generalization and learning ability.

2. Battery Aging Phenomena and Incremental Capacity Analysis

In this section, the aging test of the dataset used in this paper is presented, where aging phenomena such as voltage and capacity variations are analyzed. Subsequently, IC curves are extracted from the constant-current charging process to obtain the health indicators for SOH estimation.

2.1. Battery Aging Phenomena

To explore the aging phenomena of lithium-ion batteries, this paper begins by introducing two battery datasets obtained from the Tongji University repository [28].

Dataset 1 comprises 66 battery cells, all utilizing an 18,650-type battery with $\text{LiNi}_{0.86}\text{Co}_{0.11}\text{Al}_{0.03}\text{O}_2$ (NCA) as the cathode material, serving as the base model. This dataset is partitioned into training and test sets at a ratio of approximately 4:1 for the pre-training phase. Dataset 2 involves 55 battery cells, all utilizing an 18,650-type battery featuring $\text{LiNi}_{0.83}\text{Co}_{0.11}\text{Mn}_{0.07}\text{O}_2$ (NCM) as the cathode material, serving as the subject for transfer learning, and only 10% of 10 cells in the NCM cells are used as the training set for the transfer learning phase. All cells underwent charging with constant current and voltage, followed by discharge to a cut-off voltage after full charge. These batteries were subjected to multiple cycles in a thermostat at different charge current rates and different temperatures until the capacity decayed to 71% of the rated capacity. Each cell is denoted as CYX-Y/Z based on cycling conditions, where X indicates temperature and Y/Z indicate charge/discharge current rates. Detailed cycling conditions are provided in Table 1.

As cycles increase, the batteries exhibit varying degradation patterns. The nonlinear relationship between battery capacity and cycle count complicates SOH estimation based solely on direct physical measurements. Therefore, to enhance SOH accuracy, feature extraction from these measurements is crucial for identifying health indicators and establishing the HI-to-SOH mapping relationship.

Table 1. Cycled batteries and cycling conditions for the dataset generation.

Datasets	Cell Type	Cycling Temperature (°C)	Charge Current Rate/Discharge Rate (C)	Number of Cells	Number of Data Units
Dataset 1	NCA battery	25	0.25/1	7	2190
	Type: 18,650	25	0.5/1	19	3278
	Cutoff voltage: 2.65–4.2 V	25	1/1	9	282
	Nominal capacity: 3.5 Ah	35	0.5/1	3	1112
		45	0.5/1	28	15,777
Dataset 2	NCM battery	25	0.5/1	23	5489
	Type: 18,650	35	0.5/1	4	4712
	Cutoff voltage: 2.5–4.2 V	45	0.5/1	28	17,592
Nominal capacity: 2.5 Ah					

2.2. Incremental Capacity Curve

Using incremental capacity (IC) curve analysis during constant-current charging has been widely recognized as an effective means of analyzing battery capacity degradation. The incremental capacity is defined as dQ/dV , where Q is the capacity and V is the voltage, making it essential to monitor voltage and charging capacity throughout the constant-current charging process. Given the constancy of current during this phase, the capacity and voltage are obtained as follows [34]:

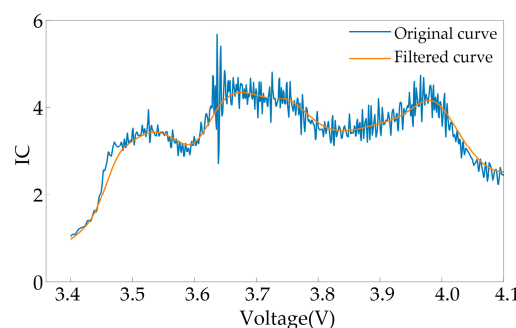
$$Q = It \quad (1)$$

$$V = f(Q), Q = f^{-1}(V) \quad (2)$$

where t represents the charging time and I denotes the charging current, thus expressing the IC curve as follows:

$$\left(f^{-1}\right)' = \frac{dQ}{dV} = \frac{I \cdot dt}{dV} = I \cdot \frac{dt}{dV} \quad (3)$$

In practical terms, IC curves derived directly from the original constant-current charging curves often exhibit considerable noise, making it challenging to establish a direct correlation with SOH. To address this issue, filtering techniques, including the moving average method and Gaussian filtering, are employed to enhance the clarity of the IC curve. These methods effectively smooth out the high-frequency noise present in the original data. Figure 1 illustrates the IC curves before and after noise reduction over one battery cycle.

**Figure 1.** Incremental capacity curves before and after noise reduction.

The IC curves of the final cyclic constant-current charging processes of NCA and NCM batteries are shown in Figure 2. When the SOH of the batteries is low, the starting voltage is close to 3.4 V. Therefore, the IC curves after 3.4 V are uniformly intercep-

ted here. A distinct trend shift direction in the IC curves reflects the phenomenon of battery capacity degradation.

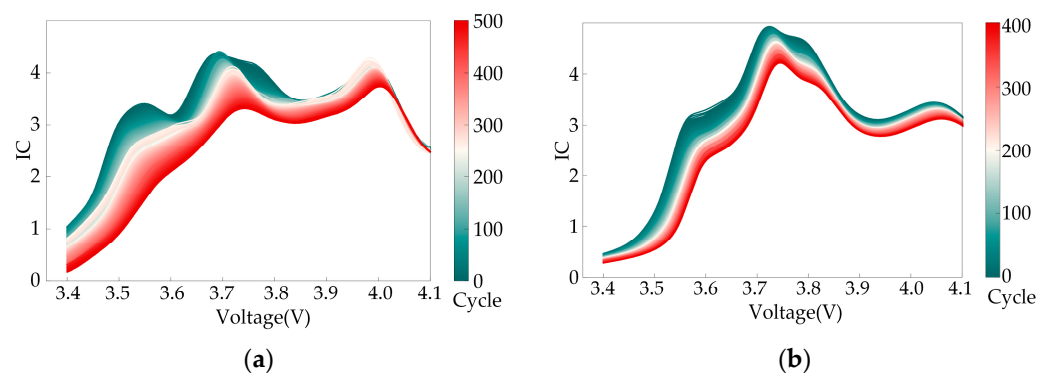


Figure 2. Incremental capacity curves: (a) NCA cells; (b) NCM cells.

However, in practical industrial applications, obtaining complete battery data is often difficult. Typically, only partial segments of data are available for analysis. Therefore, it is necessary to develop the method of estimating the capacity of lithium-ion batteries based on partial segment data. The peak of the entire IC curve is observed between 3.6 V and 3.8 V, where variations across different cycle counts become more pronounced in this voltage segment. Notably, for the NCA battery in dataset 1, the IC curves beyond 3.8 V overlap, which complicates direct analysis in that range. Therefore, the study focuses on the IC segments specifically between 3.6 V and 3.8 V, which is regarded as an important region for characterizing battery capacity degradation. The HI of SOH is extracted from this region at a 0.1 mv interval as shown in Figure 3, and finally, 20 points are obtained as model input features to evaluate the battery SOH.

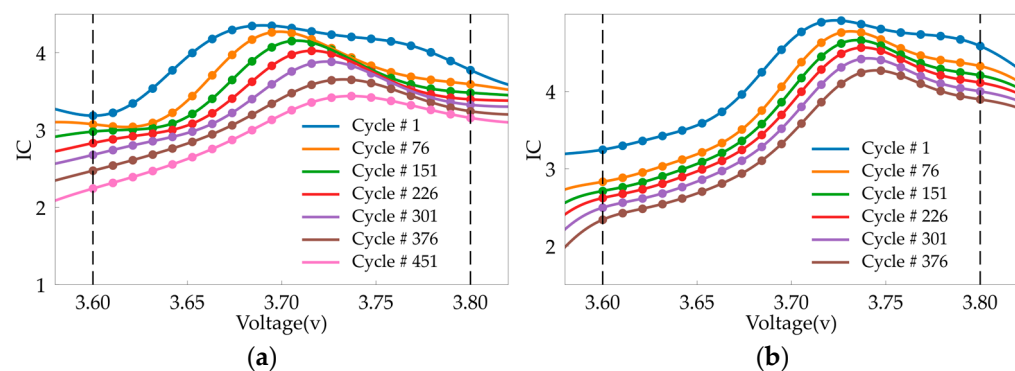


Figure 3. Features extracted from partial IC curves: (a) NCA cells; (b) NCM cells.

3. Methodology

The schematic representation of the methodology proposed in this paper is illustrated in Figure 4, comprising three main components:

(1) Extraction of features: In this study, initial physical quantities of lithium-ion batteries, such as voltage and current, are detected. In the proposed method, the voltage segment can be just part of the charging data. Subsequently, after gathering voltage and current data, the partial IC curve is computed, followed by smoothing and filtering for further analysis.

(2) The pre-training phase: The study employs a stacked bidirectional gated recurrent unit (SBiGRU) model to extract features, which are then fed into a fully connected layer for direct estimation of SOH. Additionally, Bayesian optimization and K-fold cross-validation are utilized to optimize hyperparameters, thereby enhancing the model's learning ability and generalizability.

(3) The transfer learning phase: A portion of the model parameters from the pre-training phase are frozen, and the model is fine-tuned using a limited amount of target domain data to eliminate the distributional differences of lithium-ion battery data for diverse battery types and different voltage segments under varying conditions. Bayesian optimization will adjust the number of frozen layers and the regularization factor α to optimize the performance of the transfer learning model.

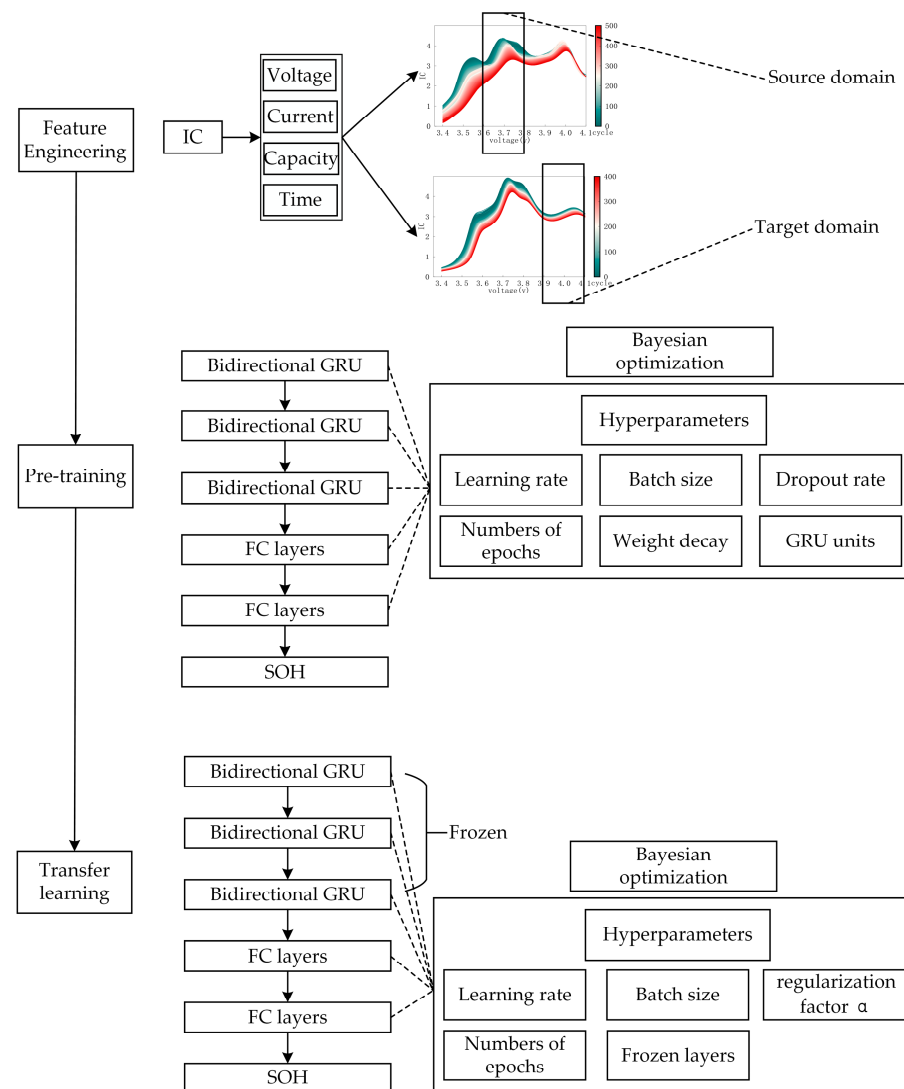


Figure 4. Overall framework of the proposed SOH estimation method.

3.1. The Gated Recurrent Unit

After extracting input features from the IC curves, a SOH estimation model must be constructed to establish the correlation between these features and SOH. This paper utilizes the gated recurrent unit (GRU), a variant of recurrent neural networks introduced by Cho et al. in 2014 [38]. GRU addresses issues such as gradient vanishing and explosion in traditional models by incorporating two control gates. It excels in modeling time series data by capturing correlations across different time scales. Figure 5 illustrates the internal structure of the GRU.

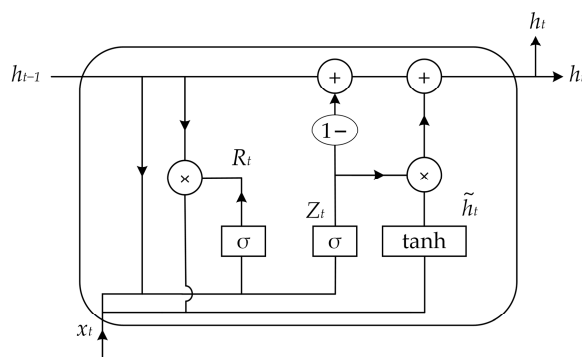


Figure 5. The gated recurrent unit structure.

When an input sequence $x = [x_1, x_2, x_3, \dots, x_{19}, x_{20}]$ consisting of partially segmented charging data first enters the reset gate R_t , R_t helps GRU determine whether or not to retain previous information to capture short-term dependencies and is implemented through a sigmoid layer [38]:

$$R_t = \sigma(W_r \cdot [h_{t-1}, x_t] + b_r) \quad (4)$$

σ represents the sigmoid activation function, h_{t-1} denotes the hidden state from the previous time step, and W_r, b_r are the weights and bias of the update gate, respectively. After the activation function, R_t is between 0 and 1. The next step is to obtain the candidate hidden state \tilde{h}_t through reset gate:

$$\tilde{h}_t = \tanh(W_h \cdot [R_t \odot h_{t-1}, x_t] + b_h) \quad (5)$$

where \tanh is the activation function of hyperbolic tangent. After the activation function \tanh , the candidate hidden state is between -1 and 1 . The parameter R_t governs the extent to which information from the preceding hidden state is preserved (closer to 1) or discarded (closer to 0). This retention mechanism influences the amount of past information carried forward to the current state. The candidate hidden state and the hidden state from the previous time step are then combined through the update gate to produce the updated hidden state. The update gate Z_t controls how much of the current input is merged into the hidden state of the output, while weighing the previous long-term memory and capturing the long-term dependencies of the sequence. The update gate Z_t and hidden state h_t expressions are as follows:

$$Z_t = \sigma(W_z \cdot [h_{t-1}, x_t] + b_z) \quad (6)$$

$$h_t = (1 - Z_t) \odot h_{t-1} + Z_t \odot \tilde{h}_t \quad (7)$$

where W_z and b_z denote the weights and bias of the update gate, respectively. As the value of Z_t gets closer to 0, the current hidden state becomes increasingly reliant on the previous hidden state, and as the value of Z_t gets closer to 1, the current hidden state is predominantly influenced by the candidate hidden state.

In this paper, the stacked bidirectional gated recurrent unit (SBiGRU) will be used for modeling. Figure 6 illustrates its bidirectional architecture [39]. This structure integrates information from both past and future contexts, achieved by stacking two independent GRUs: one processing the forward input sequence and the other the reverse input sequence. The final output is jointly determined by the hidden states of these two GRUs:

$$h_t = \delta(\vec{h}_t, \overleftarrow{h}_t) \quad (8)$$

where $\vec{h}_t, \overleftarrow{h}_t$ denote the forward hidden state and the backward hidden state, respectively. The bidirectional structure enhances the learning ability of the network and the ability to retain information from more distant moments.

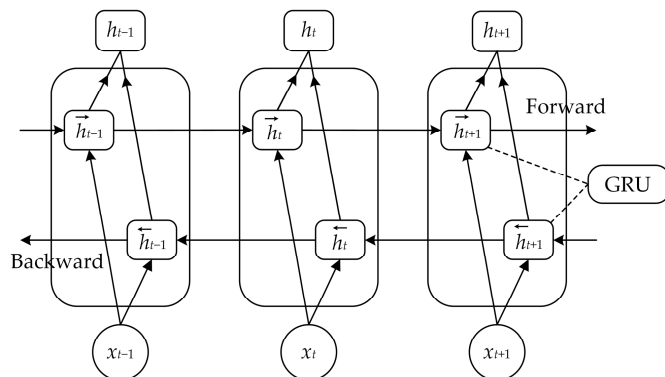


Figure 6. Bidirectional GRU neural network structure.

Stacking GRUs can construct a deeper GRU model. Within the framework of the stacked model, the output of the bidirectional hidden layer not only propagates over time but also inputs into the subsequent bidirectional hidden layer. This enables the model to capture correlations between input features across different time scales more effectively, thereby establishing nonlinear relationships between HI and SOH.

The proposed SBiGRU model is illustrated in Figure 7. In this model, the output of the final hidden layer is passed through a fully connected layer to estimate SOH using the output regression layer.

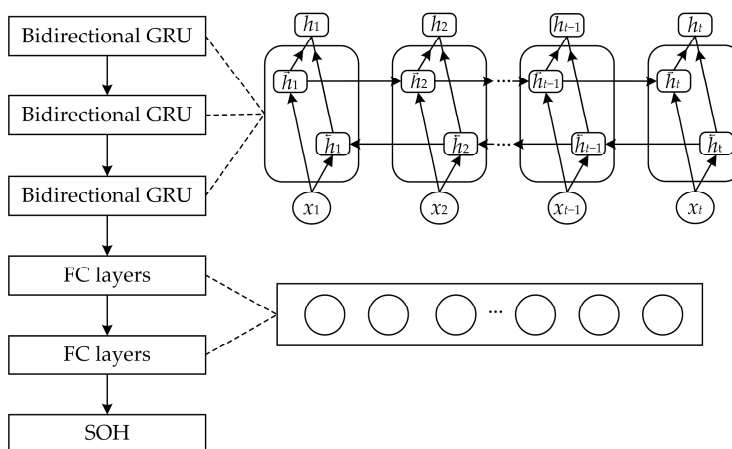


Figure 7. Overall structure of the proposed SBiGRU model.

Precautions against overfitting are necessary due to the depth of the proposed SBiGRU model. The dropout [40] and weight decay [41] techniques are combined to solve the problem. The dropout randomly masks some of the hidden neurons, which do not affect the forward propagation in the training phase, but all the neurons are involved in the output when it comes to the final testing phase. Weight decay is a regularization technique wherein the complexity of the model is reduced by penalizing smaller values of model weights. This is achieved by adding a penalty term to the loss function, typically in the form of the L2 norm of the model weights. The final loss function L is represented as follows:

$$L = L_0 + \frac{\lambda}{2} \|\mathbf{W}\|^2 \quad (9)$$

where L_0 is the original loss function value, λ is a hyperparameter responsible for controlling the strength of weight decay, and \mathbf{W} is the model weight parameter.

3.2. Hyperparameter Optimization

In neural networks, the hyperparameters are usually set manually before training. However, different combinations of hyperparameters can profoundly impact the model's learning ability and generalization. Manual adjustments inevitably reduce efficiency, and the results obtained may not be optimal. Bayesian optimization is widely recognized as an effective approach to address the black-box problem of identifying optimal hyperparameter combinations. Unlike some other optimization algorithms, Bayesian optimization focuses on the global optimum rather than the local optimum. In this paper, the hyperparameters to be optimized can be divided into those for the pre-training phase and those for the transfer learning phase. Pre-training phase hyperparameters include the number of units in each GRU hidden layer, the dropout ratio, the batch size, the learning rate, the number of epochs, and the weight decay coefficient. Transfer learning phase hyperparameters encompass the learning rate, the number of epochs, the batch size, the number of frozen layers, and the regularization term α .

Bayesian optimization obtained its name from Bayes' theorem and uses w to denote the hyperparameters to be optimized. It is assumed that it obeys the prior probability distribution $p(w)$, and the likelihood distribution of k observations at parameter w is $p(D_{1:k} | w)$, so the posterior distribution probability of w is $p(w | D_{1:k})$:

$$p(w | D_{1:k}) = \frac{p(D_{1:k} | w)p(w)}{p(D_{1:k})} \quad (10)$$

where $D_{1:k}$ denotes the observed set, the subscript $1:k$ denotes from 1 to k times and $p(D_{1:k})$ denotes the marginal likelihood distribution. Bayesian optimization comprises two main frameworks, which are the probabilistic agent model and the acquisition function. In this study, the probabilistic agent model is de-modeled by Gaussian process (GP), and the objective function $f(x)$ represents the loss function used in the SBiGRU model. It is assumed that target observation $f(x_{1:k})$ satisfies a Gaussian distribution [42]:

$$f(x_{1:k}) \sim \text{Normal}(\mu_0(x_{1:k}), \Sigma_0(x_{1:k}, x_{1:k})) \quad (11)$$

where μ_0, Σ_0 is mean function and covariance function (kernel) with learnable parameters. Then the distribution of the posterior distribution function obtained after n observations is distributed as follows:

$$f(x) | f(x_{1:n}) \sim \text{Normal}(\mu_n(x), \sigma_n^2(x)) \quad (12)$$

The expressions for its mean function and variance are as follows:

$$\mu_n(x) = \mu_0(x) + \Sigma_0(x, x_{1:n})\Sigma_0(x_{1:n}, x_{1:n})^{-1} \cdot (f(x_{1:n}) - \mu_0(x_{1:n})) \quad (13)$$

$$\sigma_n^2(x) = \Sigma_0(x, x) - \Sigma_0(x, x_{1:n}) \cdot \Sigma_0(x_{1:n}, x_{1:n})^{-1} \Sigma_0(x_{1:n}, x) \quad (14)$$

With the posterior distribution function, how to choose the next possible optimal value of the observation point x_{k+1} requires the use of the collection function. This paper adopts the strategy of expected improvement (EI), which assesses the potential improvement from the next observation relative to the current optimal solution to avoid local optima. Assuming the current optimal observation is f_k^* and $E(X)$ denotes the acquisition function, then expected improvement $EI_k(x)$ can be characterized as follows:

$$EI_k(x) = E(\max(f(x) - f_k^*, 0)) \quad (15)$$

The next observation point is then obtained from the following equation:

$$x_{k+1} = \text{argmax} EI_k(x) \quad (16)$$

In addition, to enhance the model's generalization, K-fold cross validation is implemented alongside Bayesian optimization. During training, the training data are divided into K segments for K-fold cross-validation. Each iteration uses K – 1 segments for training and the remaining segment for validation. This process is repeated K times. Specifically, in this study, K is set to 4 to ensure equal sizes for both the validation and test datasets. This approach helps in obtaining optimal hyperparameters that improve both predictive performance and model generalization.

3.3. Transfer Learning

Accurately estimating the state of health of lithium-ion batteries typically demands extensive, specific aging data for training a dedicated model. Therefore, if the distribution of this data changes, the model's estimation accuracy diminishes. Retraining the model is a common approach to mitigate this issue. This is due to variations in internal mechanisms and charging/discharging schemes among different battery types, resulting in differing data distributions. Moreover, the input features in this study comprise IC curves from specific charging segments, leading to variability in the collected data's charging segments. Direct application of the trained model for SOH estimation can result in discrepancies in domain between the source (trained model) and target domains (new SOH estimation task), leading to inaccurate capacity estimates. In this scenario, retraining the model necessitates the prior collection of sufficient new data. However, obtaining this necessary data not only consumes time but also incurs significant expenses, rendering it challenging to achieve in industrial settings. Transfer learning (TL) is more in line with practical industrial applications than traditional machine learning schemes.

Despite the domain differences between source and target data, there is always a similarity between them; leveraging information that is pertinent to the target domain in the source domain remains valuable for enhancing capacity estimation performance with limited target data. Therefore, this paper proposes a transfer learning method employing a fine-tuning strategy to pre-train the SBiGRU under the source domain and eliminate the differences between the source and target domains through parameter fine-tuning. Moreover, the robust learning capability of the base model, initially cultivated with ample source data during pre-training, can effectively enhance performance in the target domain via transfer learning.

By first freezing a part of the model parameters that have been pre-trained, training only a part of the parameters can accelerate the model convergence and effectively utilize the information gleaned from the source domain, saving training time and computational resources. Based on the specific prediction task and data distribution, the determination of which model layers to freeze (denoted as n) is automatically optimized using Bayesian optimization as described in the preceding section. Once n layers are identified, their parameters remain static throughout training to prevent updates via backward gradient propagation. Additionally, due to limited data availability in the target domain, samples from the source domain are integrated into training to help the transfer learning process. To mitigate overfitting to the source domain and ensure alignment with the target task, a regularization term α is incorporated into the loss function, resulting in the following expression:

$$L = L_0 + \frac{\alpha}{2} ||\mathbf{W} - \mathbf{W}_0||^2 \quad (17)$$

4. Discussion and Analysis of Experimental Results

To validate the effectiveness of the proposed partial incremental capacity curve and transfer learning for SOH estimation, simulation experiments will be conducted in this section using the above dataset. The hardware and software used include an Intel Core i5-12400F CPU, an NVIDIA GeForce RTX 3060Ti GPU, 32 GB of RAM, the Windows 10 operating system, Python 3.9.12, and the Pytorch environment. Prediction performance

of the model will be evaluated using root mean square error (RMSE), mean absolute percentage error (MAPE), and R^2 . These metrics are defined as follows:

$$\text{MAPE} = \frac{1}{N} \sum_{i=1}^N \frac{|y^i - \hat{y}^i|}{y^i} \times 100\% \quad (18)$$

$$\text{RMSE} = \sqrt{\frac{1}{N} \sum_{i=1}^N (y^i - \hat{y}^i)^2} \quad (19)$$

$$R^2 = 1 - \frac{\sum_{i=1}^N (\hat{y}^i - \bar{y})^2}{\sum_{i=1}^N (y^i - \bar{y})^2} \quad (20)$$

Here, y^i and \hat{y}^i are the actual and model-predicted values of SOH for the i th sample, respectively. \bar{y} denotes the sample mean and N is the number of samples. The closer the MAPE and RMSE values are to 0, the better the model prediction. Similarly, the closer the R^2 is to 1, the better the model prediction.

4.1. Pre-Training Phase

Dataset 1 is partitioned into training and test sets using the stratified sampling method, maintaining a ratio of approximately 4:1 across all experimental conditions. Additionally, a 4-fold cross-validation is employed correspondingly. Specifically, 52 cells are randomly assigned to the training set from dataset 1, while the remaining 14 cells form the test set.

4.1.1. Comparison Results of Pre-Trained Models with Different Voltage Segments

The highly nonlinear nature of the IC curve necessitates an investigation into the impact of extracting partial segment data from different voltage ranges on SOH estimation. The starting voltage of the charging process increases gradually with the number of cycles. In this study, the starting voltage is consistently set at 3.4 V, with a cutoff voltage of 4.2 V. Each voltage segment spans 0.2 V to ensure comprehensive data capture. These segments are categorized into the following ranges: 3.4–3.6 V, 3.6–3.8 V, 3.8–4.0 V, and 4.0–4.2 V. Comparative results are detailed in Table 2.

Table 2. Result comparisons of different voltage segments as a base model.

Voltage Range	MAPE	RMSE	R^2
3.4–3.6 V	0.0029	0.0033	0.9968
3.6–3.8 V	0.0061	0.0070	0.9861
3.8–4 V	0.0103	0.0116	0.9615
4–4.2 V	0.0100	0.0128	0.9529

The findings from Table 2 clearly indicate that using the voltage segment of 3.6–3.8 V as the input yields the most favorable outcomes across all three evaluation metrics, thereby affirming the superiority of this proposed input voltage segment. Additionally, it is noteworthy that the voltage segments of 3.8–4 V and 4–4.2 V exhibit comparatively lower effectiveness in contrast to the segments of 3.4–3.6 V and 3.6–3.8 V. This observation can be attributed to the overlapping phenomenon observed in the IC curves beyond 3.8 V. Figure 8 illustrates the estimated results for a randomly selected cell from the five cases in the test set. For clarity in presentation, 30 cycles of SOH values are depicted for each cell.

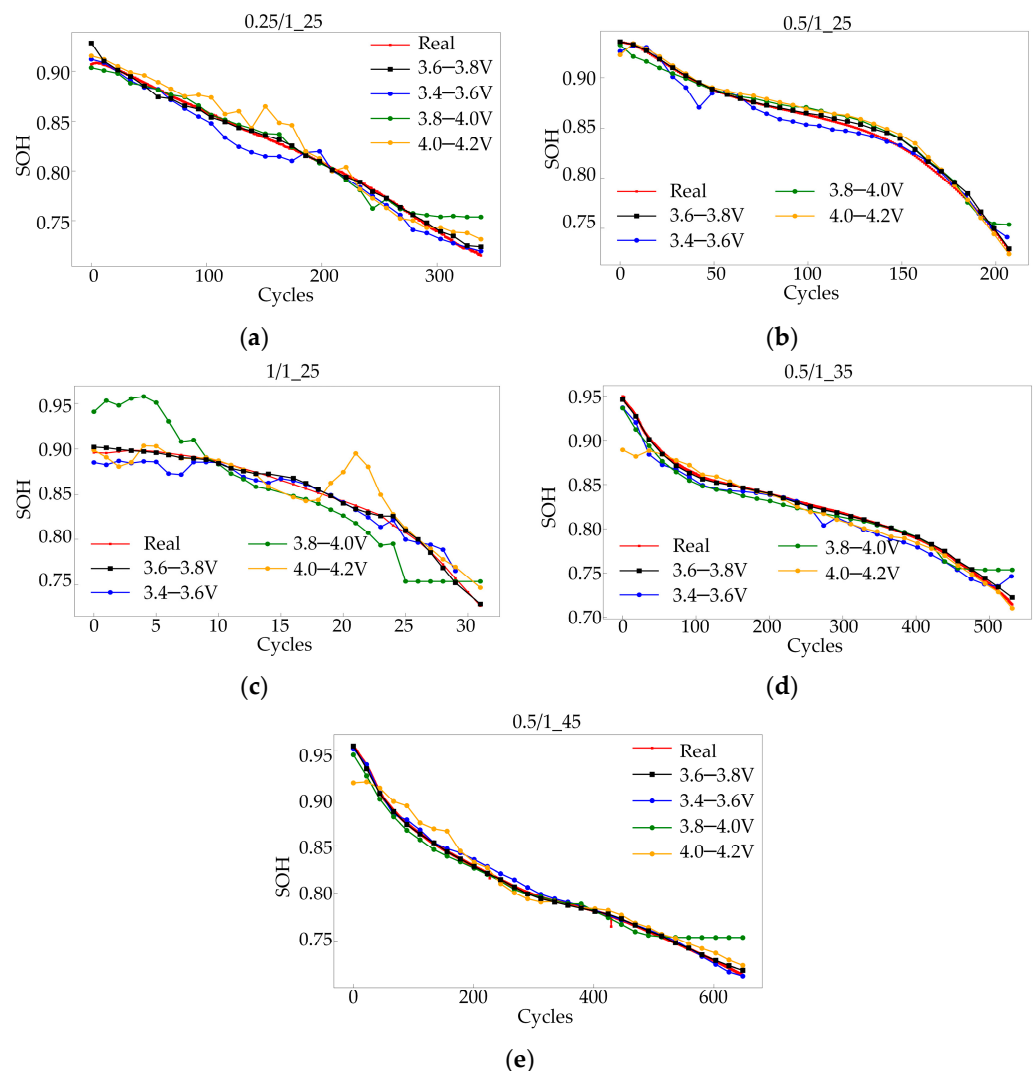


Figure 8. Estimation results for different voltage segments: (a) charge/discharge current rate of 0.25 C/1 C at 25 °C; (b) charge/discharge current rate of 0.5 C/1 C at 25 °C; (c) charge/discharge current rate of 1 C/1 C at 25 °C; (d) charge/discharge current rate of 0.5 C/1 C at 35 °C; (e) charge/discharge current rate of 0.5 C/1 C at 45 °C.

4.1.2. Comparison Results of Different Input Features

The input proposed in this study focuses on a partial segment of the capacity increment, specifically the IC value within the voltage range of 3.6–3.8 V. To ascertain the superiority of these proposed input features, they are compared against other inputs, encompassing IC values across the entire charging process as well as current and voltage data for both the entire charging duration and partial sections thereof. The results of the comparison are detailed in Table 3.

Table 3. Result comparisons of different input features.

Feature	MAPE	RMSE	R ²
Proposed	0.0029	0.0033	0.9968
Increment capacity	0.0044	0.0052	0.9924
Voltage and current	0.0117	0.0124	0.9562
Partial voltage and current	0.0087	0.0102	0.9704

The results presented in Table 3 demonstrate that using partial incremental capacity as input yields superior performance across all three evaluation metrics, thereby confirming the efficacy of the proposed input features. Furthermore, it is observed that features extracted from partial curves consistently outperform those from complete curves. This superiority may stem from redundant information in excessively long segments, which can obscure critical details in peak regions. Figure 9 illustrates the estimation outcomes for a randomly selected cell among the five cases in the test set.

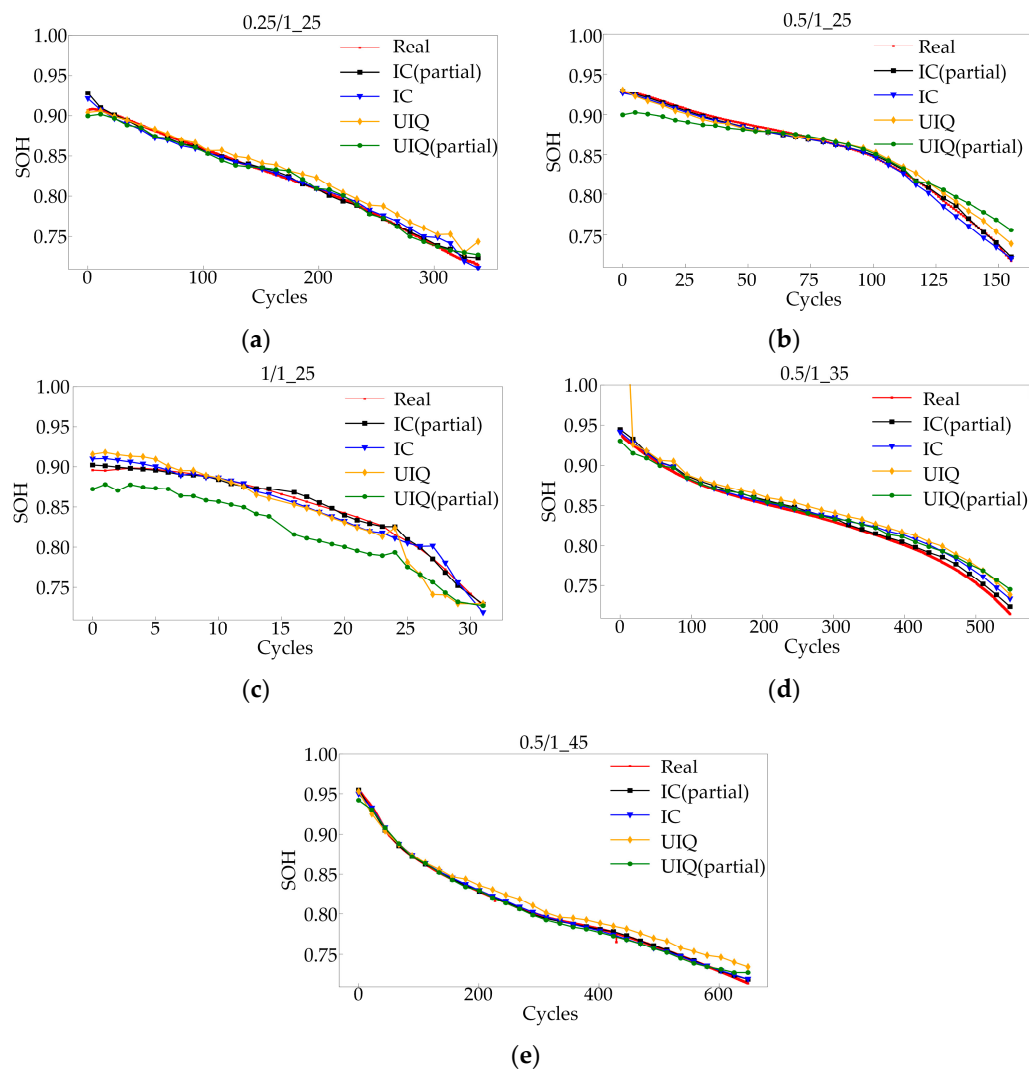


Figure 9. Estimation results for different input features: (a) charge/discharge current rate of 0.25 C/1 C at 25 °C; (b) charge/discharge current rate of 0.5 C/1 C at 25 °C; (c) charge/discharge current rate of 1 C/1 C at 25 °C; (d) charge/discharge current rate of 0.5 C/1 C at 35 °C; (e) charge/discharge current rate of 0.5 C/1 C at 45 °C.

4.1.3. Comparison Results of Different Models

To validate the efficacy of the proposed model, it is compared with other deep learning models. Features are extracted using CNN models, as well as LSTM and RNN models with the same structure as the proposed model. Furthermore, comparisons were conducted with machine learning models such as SVR and XGBoost, utilizing features extracted from the IC curves, including maximum, variance, and skewness. To ensure fairness, all models underwent hyperparameter optimization and were subjected to 4-fold cross-validation to enhance their robustness. Evaluation metrics for each model in the test are detailed in Table 4. Notably, the proposed model demonstrated outstanding performance across all

metrics, achieving a MAPE of 0.0029, an RMSE of 0.0033, and an R² of 0.9968, underscoring its effectiveness. Figure 10 depicts estimation outcomes for a randomly selected cell among the five cases in the test set.

Table 4. Result comparisons of different models.

Model	MAPE	RMSE	R ²
Proposed	0.0029	0.0033	0.9968
LSTM	0.0035	0.0045	0.9941
RNN	0.0072	0.0083	0.9805
CNN	0.0065	0.0081	0.9812
XGB	0.0093	0.0127	0.9538
SVR	0.0158	0.0258	0.8101

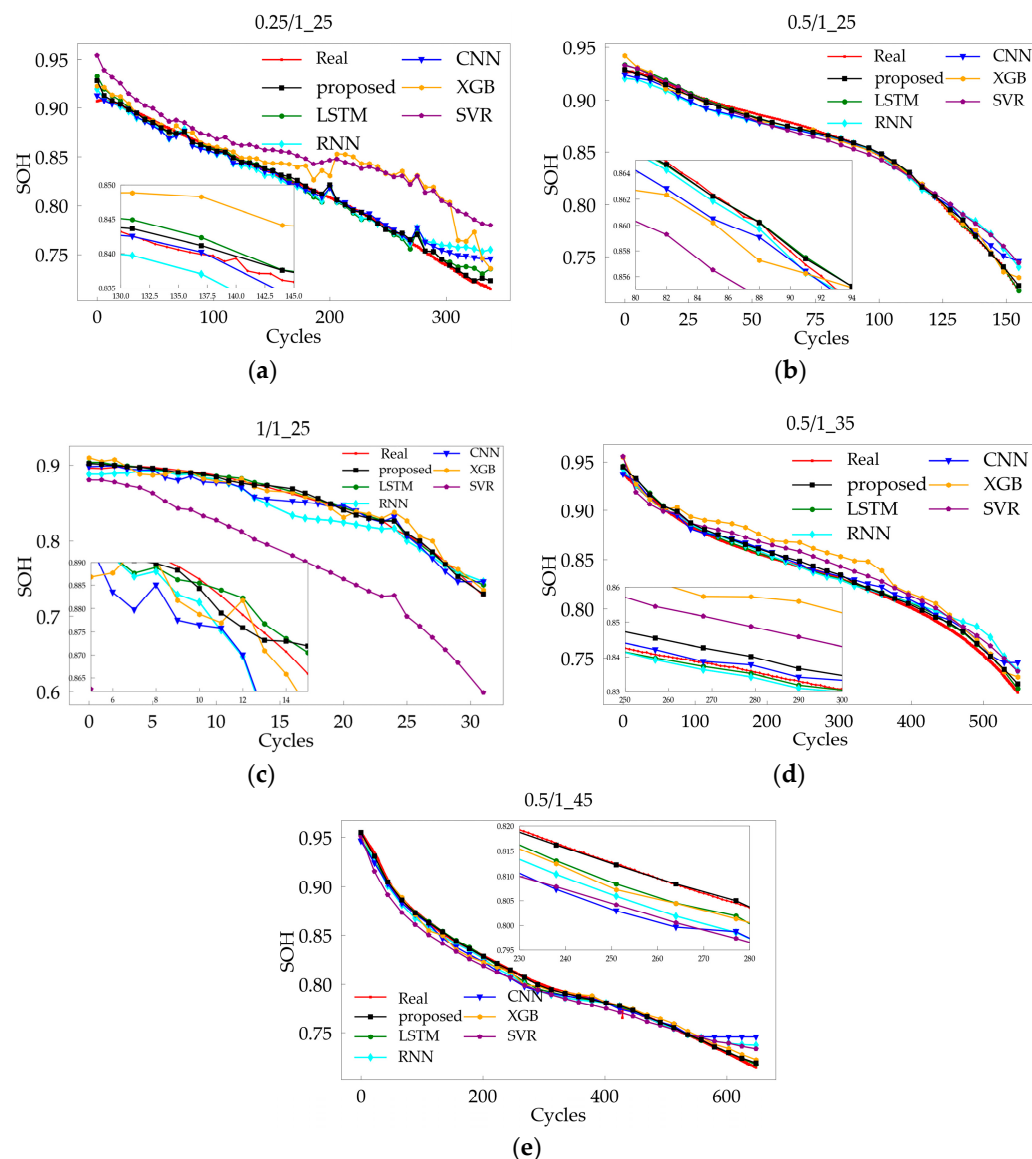


Figure 10. Estimation results for different models: (a) charge/discharge current rate of 0.25 C/1 C at 25 °C; (b) charge/discharge current rate of 0.5 C/1 C at 25 °C; (c) charge/discharge current rate of 1 C/1 C at 25 °C; (d) charge/discharge current rate of 0.5 C/1 C at 5 °C; (e) charge/discharge current rate of 0.5 C/1 C at 45 °C.

In addition, the proposed method in the pre-training phase is compared with other voltage characteristics and other state-of-the-art models proposed in the literature [28], as shown in Table 5, showing that the proposed method has better accuracy.

Table 5. RMSE of different models using different voltage-based features.

Features	Models	RMSE
Proposed	Proposed	0.0033
Relaxation voltage	XGB	0.011
Relaxation voltage	SVR	0.011
Constant current charge voltage	RF	0.010

4.2. Transfer Learning Phase

This subsection aims to validate the effectiveness of the proposed SBiGRU-TL method on the target domain dataset. The same stratified sampling method is used to divide dataset 2 into training and testing sets. To underscore the benefits of transfer learning, we designated only 10% of the 10 cells in dataset 2 as the test set, and the proportion of training samples is only 1.6% of the total samples, so as to simulate scenarios with limited data. Three methods are first compared in the transfer learning experiment:

- (1) TL: The method proposed in this paper.
- (2) Zero-TL: Following training on the source domain data, the base model weights are not changed, and the trained model is directly applied to estimate the SOH in the target domain.
- (3) No-TL: The model undergoes direct re-training using the limited target domain dataset, after which it is utilized to estimate SOH.

As shown in Table 6, the transfer learning method achieves the smallest error with a MAPE of 0.0033, an RMSE of 0.0039, and an R2 of 0.9952. In contrast, Zero-TL exhibits the worst performance, indicating the inability to directly estimate SOH in the target domain using the base model. The No-TL approach shows acceptable overall performance; however, it suffers from significant estimation errors initially, attributed to insufficient training data leading to suboptimal early-stage performance. Figure 11 presents the estimation outcomes for a randomly selected cell among the three cases in the test set.

Table 6. Result comparisons of the different methods.

Method	MAPE	RMSE	R ²
TL	0.0033	0.0039	0.9952
Zero-TL	0.0839	0.0729	-0.6431
No-TL	0.0116	0.0181	0.8984

In addition, the literature [28] proposed to add a linear transformation layer before the base model to implement transfer learning. Comparing the RMSE metrics of the proposed method in this paper, as shown in Table 7, it can be found that the proposed method also has better accuracy in the transfer learning phase.

Table 7. RMSE of different transfer learning.

Features	Models	Methods	RMSE
Proposed	Proposed	Proposed	0.0039
Relaxation voltage	XGB	Add linear layers	0.024
Relaxation voltage	SVR	Add linear layers	0.017

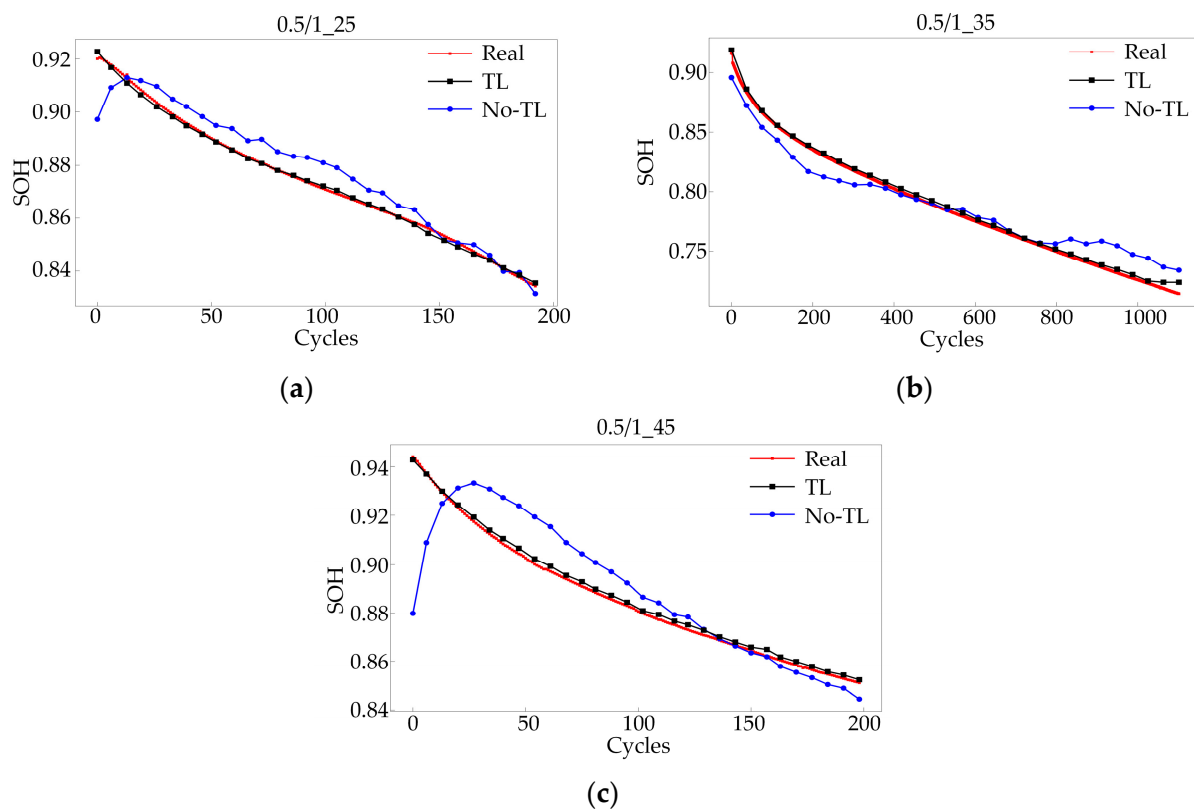


Figure 11. Estimation results for different methods: (a) charge/discharge current rate of 0.5 C/1 C at 25 °C; (b) charge/discharge current rate of 0.5 C/1 C at 35 °C; (c) charge/discharge current rate of 0.5 C/1 C at 45 °C.

In real industrial applications, obtaining desired data is not always feasible. Transfer learning offers a solution when training and test sets exhibit varying voltage ranges. Specifically, IC values from the 3.6–3.8 V voltage segment in dataset 1 serve as source domain data, while the 3.4–3.8 V, 3.6–3.8 V, 3.8–4.0 V, and 4.0–4.2 V voltage segments in dataset 2 act as target domain data. Table 8 displays the evaluation metrics for each voltage range, indicating successful estimation of SOH across varying voltage segments. Figure 12 displays the estimation outcomes for a randomly selected cell across the three cases in the test set. Notably, at a temperature of 25 degrees Celsius, voltage segments 3.4–3.6 V and 4.0–4.2 V show slightly inferior performance compared to others. This discrepancy arises from significant distribution differences between these voltage segments and the source domain data. Nevertheless, the deviation for these segments remains within 0.01.

Table 8. Transfer learning result comparisons of different voltage segments.

Voltage Range	MAPE	RMSE	R ²
3.4–3.6 V	0.0098	0.0103	0.9677
3.6–3.8 V	0.0033	0.0039	0.9952
3.8–4.0 V	0.0051	0.0059	0.9893
4.0–4.2 V	0.0079	0.0085	0.9777

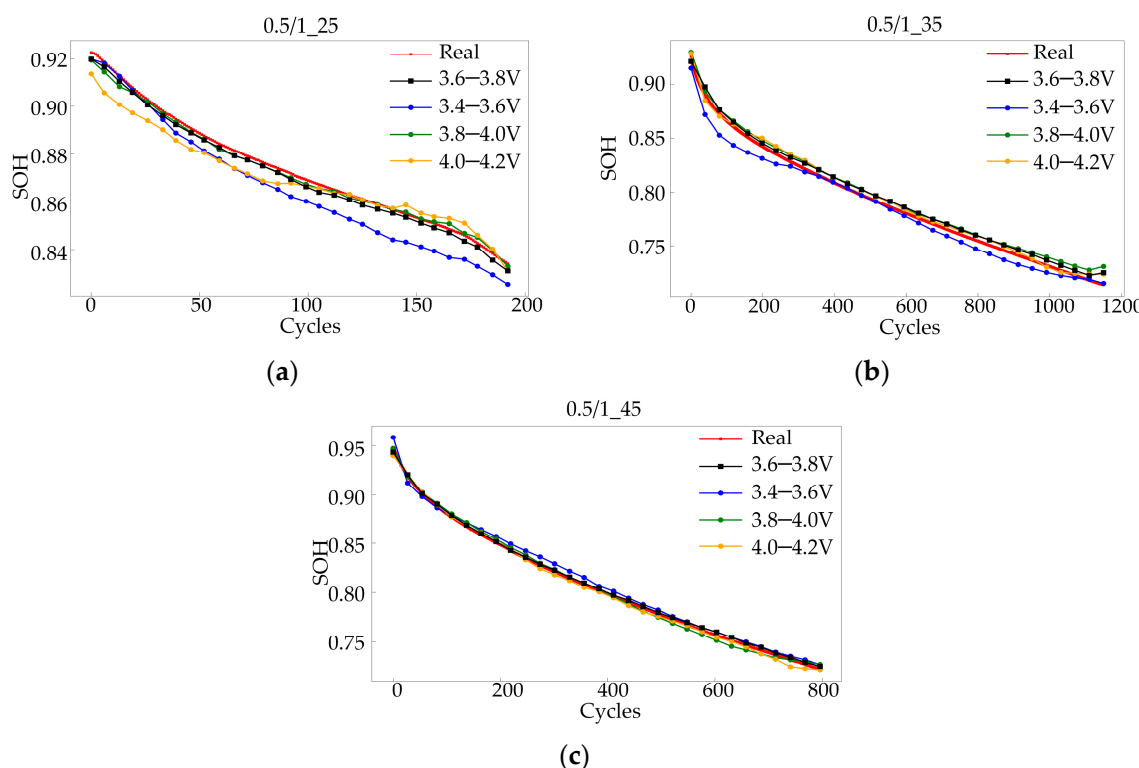


Figure 12. Estimation results for different voltage segments: (a) charge/discharge current rate of 0.5 C/1 C at 25 °C; (b) charge/discharge current rate of 0.5 C/1 C at 35 °C; (c) charge/discharge current rate of 0.5 C/1 C at 45 °C.

4.3. Discussion on Bayesian Optimization

The proposed model in this paper utilizes Bayesian optimization to optimize hyperparameters during both the pre-training and transfer learning phases. To validate the effectiveness of Bayesian optimization, the GRU is maintained with identical configuration as in the proposed model but without Bayesian optimization. Table 9 lists the hyperparameters used during the pre-training phase.

Table 9. Hyperparameters of the pre-training phase.

Hyperparameters	Without BO	With BO
Learning rate	0.001	0.00055
Batch size	64	32
Dropout rate	0.001	0.02745
Number of epochs	150	150
Weight decay	1×10^{-5}	1.32455×10^{-6}
GRU units	64,64,64	64,160,96

The hyperparameters of the transfer learning phase are shown in Table 10.

Table 10. Hyperparameters of the transfer learning phase.

Hyperparameters	Without BO	With BO
Learning rate	0.001	0.0045
Batch size	64	48
regularization factor α	1×10^{-5}	8.16×10^{-5}
Number of epochs	200	200
Frozen layers	3	1

Table 11 presents the evaluation metric values before and after optimization for both the pre-training and transfer learning phases. MAPE showed a 47% improvement and RMSE exhibited a 52% improvement. In the transfer learning phase, MAPE demonstrated a 71% improvement, while RMSE showed a 72% improvement. Figure 13 visualizes the estimation outcomes for a randomly selected cell at different phase.

Table 11. Comparative results with and without Bayesian optimization.

Phase	MAPE	RMSE	R ²
Pre-training without BO	0.0055	0.0069	0.9864
Pre-training with BO	0.0029	0.0033	0.9968
Transfer learning without BO	0.0117	0.0140	0.9427
Transfer learning with BO	0.0033	0.0039	0.9952

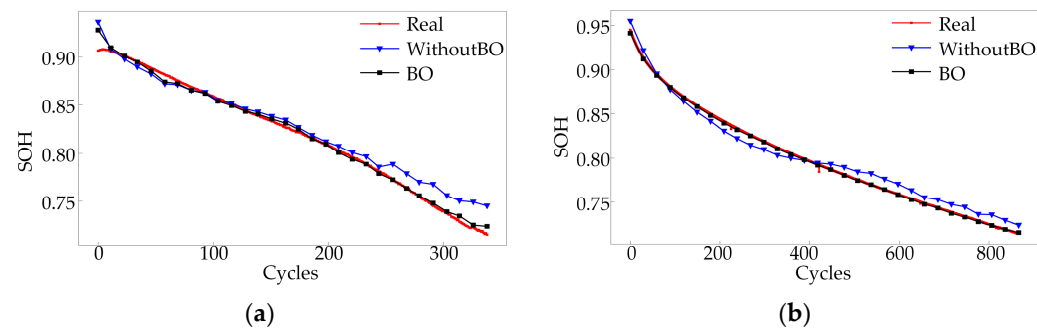


Figure 13. Comparative results with and without Bayesian optimization: (a) pre-training phase; (b) transfer learning phase.

5. Conclusions

Accurate estimation of SOH is important in battery management systems. This paper introduces a novel approach to estimating the state of health of lithium-ion batteries by leveraging partial incremental capacity curves and transfer learning. The major findings and conclusions are as follows: (1) The proposed method uses the partial incremental capacity curves as SBiGRU input to achieve SOH estimation directly. Using only partial IC curves does not rely on the complete charging process and avoids the identification of specific features. Compared with the traditional prediction model, the SBiGRU proposed in this paper has higher accuracy; (2) Considering that different types of batteries are under varying conditions and that the test data have domain differences from the training data, this paper proposes a transfer learning approach to solve this problem even when only limited data are available to accurately estimate SOH; (3) Bayesian optimization is employed to determine the number of layers to be frozen for transfer learning while optimizing the other hyperparameters of the model. Compared to relying on empirical determination of hyperparameters, this method estimates SOH more accurately.

Based on the experimental results in the dataset of Tongji University, the effectiveness and superiority of the proposed method are verified. The pre-training phase achieved MAPE and RMSE values of 0.0029 and 0.0033, respectively, while the transfer learning phase achieved 0.0033 and 0.0039. The RMSEs are also within 1% when training and test data have different voltage ranges, demonstrating robust performance. The experimental results show that the proposed method has higher accuracy and generalization compared to other methods and is suitable for industrial application scenarios.

Author Contributions: Conceptualization, S.H.; methodology, S.H. and X.W.; software, S.H.; validation, D.X., X.W. and L.K.; data curation, X.Z.; writing—original draft preparation, S.H.; writing—review and editing, X.W.; supervision, X.W., D.X. and L.K.; project administration, X.W. and L.K.; funding acquisition, L.K. All authors have read and agreed to the published version of the manuscript.

Funding: This research was funded by the Guangdong Basic and Applied Basic Research Foundation, grant number No. 2022A1515140009.

Data Availability Statement: Data used in this article are publicly available [31].

Conflicts of Interest: Author Di Xie was employed by the company Guangdong Hynn Technology Co., Ltd. The remaining authors declare that the research was conducted in the absence of any commercial or financial relationships that could be construed as a potential conflict of interest.

References

1. Blomgren, G.E. The development and future of lithium ion batteries. *J. Electrochem. Soc.* **2016**, *164*, A5019. [[CrossRef](#)]
2. Bresser, D.; Hosoi, K.; Howell, D.; Li, H.; Zeisel, H.; Amine, K.; Passerini, S. Perspectives of automotive battery R&D in China, Germany, Japan, and the USA. *J. Power Sources* **2018**, *382*, 176–178.
3. Waag, W.; Käbitz, S.; Sauer, D.U. Experimental investigation of the lithium-ion battery impedance characteristic at various conditions and aging states and its influence on the application. *Appl. Energy* **2013**, *102*, 885–897. [[CrossRef](#)]
4. Ng, K.S.; Moo, C.-S.; Chen, Y.-P.; Hsieh, Y.-C. Enhanced coulomb counting method for estimating state-of-charge and state-of-health of lithium-ion batteries. *Appl. Energy* **2009**, *86*, 1506–1511. [[CrossRef](#)]
5. Xiong, R.; Li, L.; Tian, J. Towards a smarter battery management system: A critical review on battery state of health monitoring methods. *J. Power Sources* **2018**, *405*, 18–29. [[CrossRef](#)]
6. Lyu, C.; Song, Y.; Zheng, J.; Luo, W.; Hinds, G.; Li, J.; Wang, L. In situ monitoring of lithium-ion battery degradation using an electrochemical model. *Appl. Energy* **2019**, *250*, 685–696. [[CrossRef](#)]
7. Hu, X.; Che, Y.; Lin, X.; Onori, S. Battery health prediction using fusion-based feature selection and machine learning. *IEEE Trans. Transp. Electrif.* **2020**, *7*, 382–398. [[CrossRef](#)]
8. Cai, L.; Lin, J.; Liao, X. A data-driven method for state of health prediction of lithium-ion batteries in a unified framework. *J. Energy Storage* **2022**, *51*, 104371. [[CrossRef](#)]
9. Lai, X.; Yi, W.; Cui, Y.; Qin, C.; Han, X.; Sun, T.; Zhou, L.; Zheng, Y. Capacity estimation of lithium-ion cells by combining model-based and data-driven methods based on a sequential extended Kalman filter. *Energy* **2021**, *216*, 119233. [[CrossRef](#)]
10. Tang, X.; Liu, K.; Wang, X.; Liu, B.; Gao, F.; Widanage, W.D. Real-time aging trajectory prediction using a base model-oriented gradient-correction particle filter for Lithium-ion batteries. *J. Power Sources* **2019**, *440*, 227118. [[CrossRef](#)]
11. Chen, Z.; Sun, M.; Shu, X.; Xiao, R.; Shen, J. Online state of health estimation for lithium-ion batteries based on support vector machine. *Appl. Sci.* **2018**, *8*, 925. [[CrossRef](#)]
12. Feng, X.; Weng, C.; He, X.; Han, X.; Lu, L.; Ren, D.; Ouyang, M. Online state-of-health estimation for Li-ion battery using partial charging segment based on support vector machine. *IEEE Trans. Veh. Technol.* **2019**, *68*, 8583–8592. [[CrossRef](#)]
13. Richardson, R.R.; Osborne, M.A.; Howey, D.A. Gaussian process regression for forecasting battery state of health. *J. Power Sources* **2017**, *357*, 209–219. [[CrossRef](#)]
14. Richardson, R.R.; Birk, C.R.; Osborne, M.A.; Howey, D.A. Gaussian process regression for in situ capacity estimation of lithium-ion batteries. *IEEE Trans. Ind. Inform.* **2018**, *15*, 127–138. [[CrossRef](#)]
15. Wang, J.; Deng, Z.; Li, J.; Peng, K.; Xu, L.; Guan, G.; Abudula, A. State of Health Trajectory Prediction Based on Multi-Output Gaussian Process Regression for Lithium-Ion Battery. *Batteries* **2022**, *8*, 134. [[CrossRef](#)]
16. Chaoran, L.; Fei, X.; Yaxiang, F.; Guorun, Y.; Xin, T. An approach to lithium-ion battery SOH estimation based on convolutional neural network. *Trans. China Electrotech. Soc.* **2020**, *35*, 4106–4119.
17. Cao, M.; Zhang, T.; Wang, J.; Liu, Y. A deep belief network approach to remaining capacity estimation for lithium-ion batteries based on charging process features. *J. Energy Storage* **2022**, *48*, 103825. [[CrossRef](#)]
18. Shen, S.; Sadoughi, M.; Chen, X.; Hong, M.; Hu, C. A deep learning method for online capacity estimation of lithium-ion batteries. *J. Energy Storage* **2019**, *25*, 100817. [[CrossRef](#)]
19. Fan, Y.; Xiao, F.; Li, C.; Yang, G.; Tang, X. A novel deep learning framework for state of health estimation of lithium-ion battery. *J. Energy Storage* **2020**, *32*, 101741. [[CrossRef](#)]
20. Gu, X.; See, K.W.; Li, P.; Shan, K.; Wang, Y.; Zhao, L.; Lim, K.C.; Zhang, N.J.E. A novel state-of-health estimation for the lithium-ion battery using a convolutional neural network and transformer model. *Energy* **2023**, *262*, 125501. [[CrossRef](#)]
21. Li, W.; Sengupta, N.; Dechent, P.; Howey, D.; Annaswamy, A.; Sauer, D.U. Online capacity estimation of lithium-ion batteries with deep long short-term memory networks. *J. Power Sources* **2021**, *482*, 228863. [[CrossRef](#)]
22. Liu, K.; Kang, L.; Xie, D. Online state of health estimation of lithium-ion batteries based on charging process and long short-term memory recurrent neural network. *Batteries* **2023**, *9*, 94. [[CrossRef](#)]
23. Lin, H.; Kang, L.; Xie, D.; Linghu, J.; Li, J. Online state-of-health estimation of lithium-ion battery based on incremental capacity curve and BP neural network. *Batteries* **2022**, *8*, 29. [[CrossRef](#)]
24. Wei, Y.; Wu, D.J.R.E.; Safety, S. Prediction of state of health and remaining useful life of lithium-ion battery using graph convolutional network with dual attention mechanisms. *Reliab. Eng. Syst. Saf.* **2023**, *230*, 108947. [[CrossRef](#)]
25. Xiong, R.; Zhang, Y.; Wang, J.; He, H.; Peng, S.; Pecht, M. Lithium-ion battery health prognosis based on a real battery management system used in electric vehicles. *IEEE Trans. Veh. Technol.* **2018**, *68*, 4110–4121. [[CrossRef](#)]
26. Lu, C.; Tao, L.; Fan, H. Li-ion battery capacity estimation: A geometrical approach. *J. Power Sources* **2014**, *261*, 141–147. [[CrossRef](#)]

27. Liu, J.; Chen, Z. Remaining useful life prediction of lithium-ion batteries based on health indicator and Gaussian process regression model. *IEEE Access* **2019**, *7*, 39474–39484. [[CrossRef](#)]
28. Zhu, J.; Wang, Y.; Huang, Y.; Bhushan Gopaluni, R.; Cao, Y.; Heere, M.; Mühlbauer, M.J.; Mereacre, L.; Dai, H.; Liu, X. Data-driven capacity estimation of commercial lithium-ion batteries from voltage relaxation. *Nat. Commun.* **2022**, *13*, 2261. [[CrossRef](#)]
29. Li, X.; Jiang, J.; Chen, D.; Zhang, Y.; Zhang, C. A capacity model based on charging process for state of health estimation of lithium ion batteries. *Appl. Energy* **2016**, *177*, 537–543. [[CrossRef](#)]
30. Chang, C.; Wang, Q.; Jiang, J.; Wu, T. Lithium-ion battery state of health estimation using the incremental capacity and wavelet neural networks with genetic algorithm. *J. Energy Storage* **2021**, *38*, 102570. [[CrossRef](#)]
31. Li, X.; Yuan, C.; Wang, Z. State of health estimation for Li-ion battery via partial incremental capacity analysis based on support vector regression. *Energy* **2020**, *203*, 117852. [[CrossRef](#)]
32. Weng, C.; Feng, X.; Sun, J.; Peng, H. State-of-health monitoring of lithium-ion battery modules and packs via incremental capacity peak tracking. *Appl. Energy* **2016**, *180*, 360–368. [[CrossRef](#)]
33. Li, X.; Wang, Z.; Zhang, L.; Zou, C.; Dorrell, D.D. State-of-health estimation for Li-ion batteries by combing the incremental capacity analysis method with grey relational analysis. *J. Power Sources* **2019**, *410*, 106–114. [[CrossRef](#)]
34. Li, X.; Yuan, C.; Li, X.; Wang, Z. State of health estimation for Li-Ion battery using incremental capacity analysis and Gaussian process regression. *Energy* **2020**, *190*, 116467. [[CrossRef](#)]
35. Deng, Z.; Hu, X.; Li, P.; Lin, X.; Bian, X. Data-driven battery state of health estimation based on random partial charging data. *IEEE Trans. Power Electron.* **2021**, *37*, 5021–5031. [[CrossRef](#)]
36. Meng, H.; Geng, M.; Han, T. Long short-term memory network with Bayesian optimization for health prognostics of lithium-ion batteries based on partial incremental capacity analysis. *Reliab. Eng. Syst. Saf.* **2023**, *236*, 109288. [[CrossRef](#)]
37. Qian, C.; Xu, B.; Chang, L.; Sun, B.; Feng, Q.; Yang, D.; Ren, Y.; Wang, Z. Convolutional neural network based capacity estimation using random segments of the charging curves for lithium-ion batteries. *Energy* **2021**, *227*, 120333. [[CrossRef](#)]
38. Cho, K.; Van Merriënboer, B.; Gulcehre, C.; Bahdanau, D.; Bougares, F.; Schwenk, H.; Bengio, Y. Learning phrase representations using RNN encoder-decoder for statistical machine translation. *arXiv* **2014**, arXiv:1406.1078.
39. Bian, C.; He, H.; Yang, S. Stacked bidirectional long short-term memory networks for state-of-charge estimation of lithium-ion batteries. *Energy* **2020**, *191*, 116538. [[CrossRef](#)]
40. Wei, M.; Gu, H.; Ye, M.; Wang, Q.; Xu, X.; Wu, C. Remaining useful life prediction of lithium-ion batteries based on Monte Carlo Dropout and gated recurrent unit. *Energy Rep.* **2021**, *7*, 2862–2871. [[CrossRef](#)]
41. Zhang, Y.; Xiong, R.; He, H.; Pecht, M.G. Long short-term memory recurrent neural network for remaining useful life prediction of lithium-ion batteries. *IEEE Trans. Veh. Technol.* **2018**, *67*, 5695–5705. [[CrossRef](#)]
42. Yang, L.; Shami, A. On hyperparameter optimization of machine learning algorithms: Theory and practice. *Neurocomputing* **2020**, *415*, 295–316. [[CrossRef](#)]

Disclaimer/Publisher's Note: The statements, opinions and data contained in all publications are solely those of the individual author(s) and contributor(s) and not of MDPI and/or the editor(s). MDPI and/or the editor(s) disclaim responsibility for any injury to people or property resulting from any ideas, methods, instructions or products referred to in the content.